Dielectric nano-antennas for strain engineering in atomically thin two-dimensional semiconductors

Luca Sortino,[1,*] Matthew Brooks,[2] Panaiot G. Zotev,[1] Armando Genco,[1] Javier Cambiasso,[3] Sandro Mignuzzi,[3] Stefan A. Maier,[3,4] Guido Burkard,[2] Riccardo Sapienza,[3] and Alexander I. Tartakovskii[1,†]

[1] *Department of Physics and Astronomy, University of Sheffield, Sheffield, S3 7RH, United Kingdom*
[2] *Department of Physics, University of Konstanz, D-78464 Konstanz, Germany*
[3] *The Blackett Laboratory, Department of Physics, Imperial College London, London, SW7 2BW, United Kingdom*
[4] *Chair in Hybrid Nanosystems, Nanoinstitute Münich, Faculty of Physics, Ludwig-Maximilians-Universität München, 80539 Münich, Germany*

(Dated: February 12, 2020)

Atomically thin two-dimensional semiconducting transition metal dichalcogenides (TMDs) can withstand large levels of strain before their irreversible damage occurs. This unique property offers a promising route for control of the optical and electronic properties of TMDs, for instance by depositing them on nano-structured surfaces, where position-dependent strain can be produced on the nano-scale. Here, we demonstrate strain-induced modifications of the optical properties of mono- and bilayer TMD WSe_2 placed on photonic nano-antennas made from gallium phosphide (GaP). Photoluminescence (PL) from the strained areas of the TMD layer is enhanced owing to the efficient coupling with the confined optical mode of the nano-antenna. Thus, by following the shift of the PL peak, we deduce the changes in the strain in WSe_2 deposited on the nano-antennas of different radii. In agreement with the presented theory, strain up to $\approx 1.4\%$ is observed for WSe_2 monolayers. We also estimate that $> 3\%$ strain is achieved in bilayers, accompanied with the emergence of a direct bandgap in this normally indirect-bandgap semiconductor. At cryogenic temperatures, we find evidence of the exciton confinement in the most strained nano-scale parts of the WSe_2 layers, as also predicted by our theoretical model. Our results, of direct relevance for both dielectric and plasmonic nano-antennas, show that strain in atomically thin semiconductors can be used as an additional parameter for engineering light-matter interaction in nano-photonic devices.

Control over lattice distortions in semiconductors, or strain-engineering, offers valuable tools for tailoring their electronic and optical properties [1]. The exceptional flexibility of atomically thin two-dimensional (2D) crystals [2] has opened the way to employ mechanical deformation for engineering their physical properties [3–8], and has made them promising for applications in flexible electronics [9]. Among 2D semiconductors, the family of transition metal dichalcogenides [10, 11] has shown attractive properties including an indirect-to-direct bandgap transition in monolayers [12, 13], tightly bound excitons [14, 15] and coupling between the spin and valley degrees of freedom [16]. Single layers of TMDs, only three atoms thick, have been observed to withstand large strain levels (>10%)[17] before fracture, offering a unique possibility to engineer their electronic band structure using strain [18–21]. This approach has been successfully applied for modifying their optical properties [22–26], tuning carrier mobilities [27] and controlling the charge transport [28, 29]. Furthermore, spatial variation of the strain in TMD layers, occurring due to imperfections of fabrication methods or introduced intentionally, translates into a position dependent bandgap [30]. This was shown to result in periodically modulated optical properties in monolayer MoS_2 placed on pre-patterned substrates [31], as well as to give rise to funnelling of excitons into the areas with a larger tensile strain [32, 33], where the lowest exciton energy is achieved. Finally, in mono- and bi-layer WSe_2 and WS_2 placed on silica or polymer nano-pillars, single photon emitting defects were readily observed, whose origin was thus linked with the strain induced in the few-layer semiconductor [34, 35].

While initial demonstrations of strained 2D semiconductors in electronic devices have been reported [27, 36], the use of strain to control the optical properties of TMDs in nano-photonic systems has been largely unexplored [37]. One of the approaches to engineer light-matter interaction relies on the use of nano-antennas [38–40], which can confine light in volumes below the diffraction limit [41]. The strong confinement of the electric field at the hot-spots of the nano-antenna, enhances the light-matter interaction for the emitters positioned within the volume of its optical mode [5, 43, 44]. While these phenomena have been extensively studied for surface plasmons in metals [45–47], recently high-refractive-index dielectric nano-photonic structures [48] have rapidly gained attention as they offer low losses [49, 50] and both electric and magnetic Mie-type optical resonances [51]. Recent reports of dielectric nano-antennas interfaced with 2D TMDs showed modified PL directionality in monolayer MoS_2 coupled to silicon nano-rods [52], as well as strong PL and Raman signal enhancement for WSe_2 placed on top of GaP pillars [5]. The latter case is further investigated in this work.

Contrary to previous approaches employing bending apparatus [22], piezoelectric substrates [53] or relying

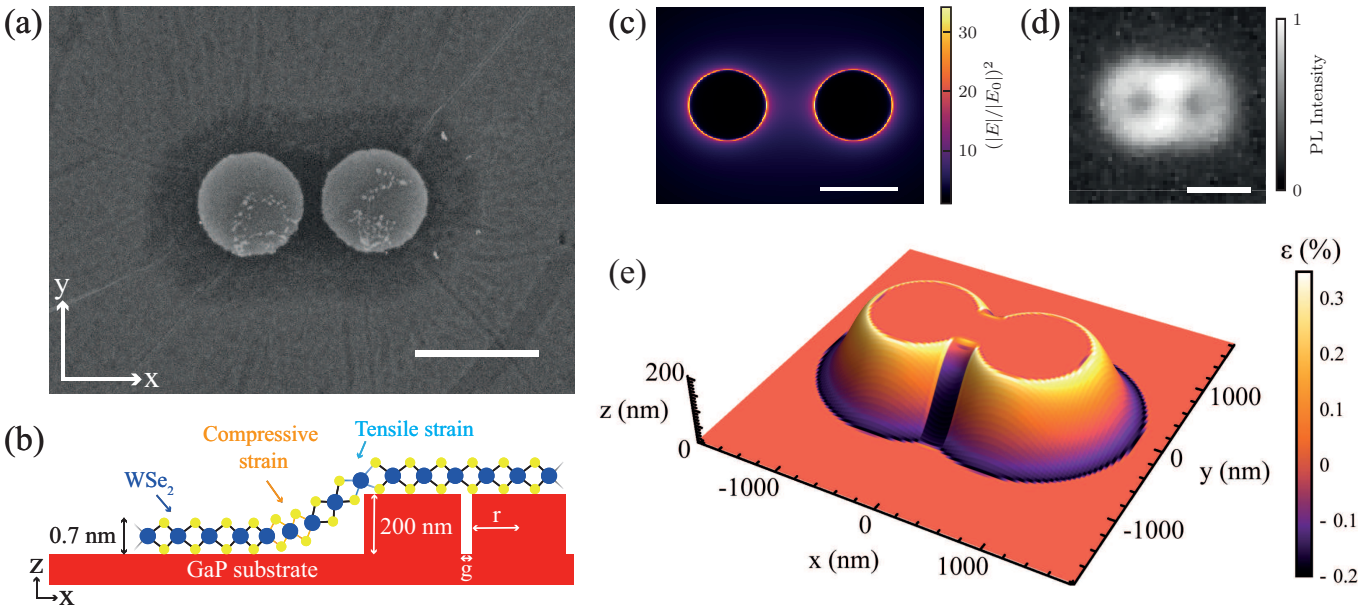

FIG. 1. (a) Scanning electron microscope image of a GaP dimer nano-antenna (top view) with a radius r=400 nm, covered with 2L-WSe_2. Scale bar: 1 μm. The darker area around the nano-pillars is the suspended 2D layer stretching from the substrate up to the top surface of the nano-antenna. (b) Schematic of a GaP dimer nano-antenna shown in red with a monolayer of WSe_2 transferred on its top. The areas of high compressive and tensile strain are labelled. (c) The ratio of the intensities of the scattered and incident electro-magnetic waves shown as the ratio of the corresponding electric fields $(|E|/|E_0|)^2$ for a GaP dimer nano-antenna with r=50 nm under 685 nm unpolarized excitation. The presented field distribution is calculated at the top of the dimer (z=200 nm) with a finite-difference time-domain software (Lumerical Inc.). Scale bar: 100 nm. (d) Photoluminescence image of a GaP nano-antenna (r = 300 nm) covered with monolayer WSe_2. The brightest PL is observed where the tensile strain and near-field enhancement are co-located and maximized. Scale bar: 600 nm. (e) Calculated strain ε for a monolayer WSe_2 placed on top of a dimer nano-antenna with r = 500 nm. The middle of the gap corresponds to x=0 and y=0.

on the difference of the thermal expansion coefficients [54, 55], here we demonstrate that a single nano-antenna can be used to strain a 2D semiconducting layer, while at the same time the PL from the strained material is enhanced via the coupling with the optical mode of the nano-antenna [5]. We study both experimentally and theoretically monolayers (1L) and bilayers (2L) of TMD WSe_2 transferred on closely spaced (<100 nm) pairs of nano-pillars, referred to as dimers [5, 56] below (see Figs.1a-d). The co-location between WSe_2 tensile deformation and the maximum of the near-field enhancement of the antenna at the edges of the top surface of the pillars (Fig.1b-e), allows clear observation of the strain-induced band structure modifications in PL. We demonstrate a dependence of the amount of strain induced in the TMD layer by nano-antennas of different radii. With this approach we observe the tuning of the intralayer exciton in monolayer WSe_2 exceeding 50 meV, corresponding to the uniaxial tensile strain up to $\approx 1.4\%$ [57]. These findings are supported by our model based on the continuum-mechanical plate theory approach [1, 2], which we use to calculate the strain distribution in 1L and 2L-WSe_2 placed on the nano-antennas. Using this theory we predict higher strain in the bilayers than in monolayers placed on the nano-antennas of the same radius. Tensile strain $> 3\%$ is calculated for 2L-WSe_2 placed on the nano-antenna with r = 50 nm, for which we experimentally observe abrupt changes in the PL spectrum consistent with the transition to the direct bandgap. From the calculated topography model, we deduce the position-dependent band structure induced in the WSe_2 and predict occurrence of strain-induced potential wells at the nano-pillar edges, which can trap the excitons. This behaviour is confirmed in the cryogenic PL measurements of 2L-WSe_2, which exhibits localization of the excitonic PL, consistent with the predicted potential shape. Further to demonstrating tuning of strain in TMDs using all-dielectric nano-antennas of various dimensions, our findings have direct relevance to TMDs coupled to plasmonic structures, where similarly both the strain and the enhanced optical fields may be co-located [60, 61].

RESULTS

Strained WSe_2 coupled with GaP nano-antennas Fig.1a shows an electron microscopy image of the top view of a GaP dimer nano-antenna with an atomically thin WSe_2 bilayer deposited on top. Owing to its elasticity, the thin semiconductor crystal stretches from the substrate up to the topmost edge of the nano-antenna, without compromising its integrity. Fig.1b shows a schematic diagram of a WSe_2 monolayer (0.7 nm thick) transferred on top of a GaP dimer nano-antenna. We use nano-antennas with a height of 200 nm, a radius varying from 50 to 500 nm and a gap from 50-100 nm. Due to the height mismatch between the substrate and the top surface of the antenna, the WSe_2 layer experiences a local compressive or tensile deformation, as shown in Fig.1b,e. Under illumination, the dimer nano-antenna exhibits confined optical resonances [5, 56]. Fig.1c shows the electric field distribution, $(|E|/|E_0|)^2$, at the top surface of a GaP dimer nano-antenna under unpolarized excitation. Here, E is the scattered field by the nano-antenna and E_0 the electric field of the plane wave illuminating the structure. Maxima of the field intensity are located at the edges of each nano-pillar and inside the gap region between them. The transferred 2D semiconductor layer stretches over the nano-structure, fully overlapping with the confined optical modes [5]. An optical microscope image of 1L-WSe_2 PL emission on top of a single GaP dimer nano-antenna, with $r = 300$ nm and $g = 65$ nm, is shown in Fig.1d (see Methods and Ref.[62] for more details). In this image it is possible to resolve the spatial distribution of the PL signal which closely resembles that of the enhanced field in Fig.1c.

We describe the nano-scale distortions in the 2D layer with an approach based on the continuum-mechanical plate theory [1] by modelling the pressure experienced by the stretched semiconductor in the out-of-plane direction (see Supplementary Note I for the full description). From the analytically calculated function for a single pillar, we interpolate to the low-symmetry dimer structure and calculate the spatial distribution of strain introduced in the stretched semiconductor crystal. The resulting strain topography for a 1L-WSe_2 placed on top of a dimer nano-antenna is shown in Fig.1e. The tensile strain reaches its maximum at the topmost edge of each nano-pillar, at a height $z = 200$ nm, co-located with the largest near-field enhancement produced by the underlying nano-antenna. The regions of compressive strain are located where the 2D layer touches the substrate, at $z \approx 0$, and inside the gap region between the pillars.

In what follows, we show that the co-location of the maximum of the confined optical mode and that of the tensile deformation in the 2D layer, allows us to directly probe the strain-induced band structure renormalization by monitoring the enhanced excitonic room temperature PL emission for both 1L and 2L-WSe_2. At cryogenic temperature, we show the exciton PL localization in 2L-WSe_2 in the regions of the largest tensile strain where the reduction of the exciton energy is the strongest as predicted by our theoretical model leading to the exciton funnelling effect [32].

Strain tuning in 1L-WSe_2 coupled to GaP nano-antennas We studied the emission from the same nano-antenna shown in Fig.1 in a micro-PL setup at room temperature using PL mapping with a micron resolution (see Methods), as shown in Fig.2a. The sample is excited at $\lambda_{exc} = 685$ nm, below the absorption edge of GaP, and thus this light is only absorbed by the WSe_2 layer. As expected, a large enhancement in the overall WSe_2 PL intensity is correlated with the location of the nano-antenna. Note, that in contrast to Fig.1d, here the resolution is limited by the excitation spot size ($r \approx 1$ μm). As shown in Fig.2b, we extract the peak maxima from the PL map in Fig.2a and observe a prominent red-shift of the intralayer exciton (also referred to as 'A exciton') peak on the nano-antenna. This effect is expected from the reduction of the WSe_2 bandgap under tensile strain. As schematically shown in Fig.2c, the direct optical transition in 1L-WSe_2 is located at the K(K') point of the Brillouin zone [12, 13]. Under the increasing tensile strain, the bandgap is expected to reduce [25, 26] mainly due to the lowering of the conduction band minimum, as a consequence of the change in the electronic orbital overlap following the the changes in the atomic bond lengths and angles [19, 20, 63]. Strain induced by underlying nano-structures has previously been measured using Raman enhancement in graphene on plasmonic nano-antennas[64, 65]. As we show in Supplementary Note II, we collected the Raman scattering signal from the strained 1L-WSe_2 and observe a shift of the Raman peak, as expected for tensile strain [4].

From our theoretical description we have derived a dependence of the tensile strain maximum, located at the nano-pillar edges, on the nano-antenna size (see Supplementary Fig.S1). We found that by reducing the nano-pillar radius an increased strain is introduced in the 2D layer. We confirm this trend experimentally in Fig.2d which shows the normalized 1L-WSe_2 PL spectra for the TMD coupled to nano-antennas of different radii. For comparison we also show the PL spectrum for WSe_2 on a planar GaP substrate, where the intralayer exciton peak is marked by a dashed line. When the nano-pillar radius is reduced, the larger red-shift in the exciton PL peak confirms that the semiconducting layer is experiencing an increased strain, as predicted by our model.

By using the previously experimentally observed gauge value for the WSe_2 intralayer A exciton red-shift as a function of strain of -49 ± 2 meV/% [57], we extract the uniaxial tensile strain magnitude for WSe_2 placed on the nano-antennas with different radii. As shown in Fig.2e, we find tensile strain values up to $\approx 1.4\%$ as the nano-

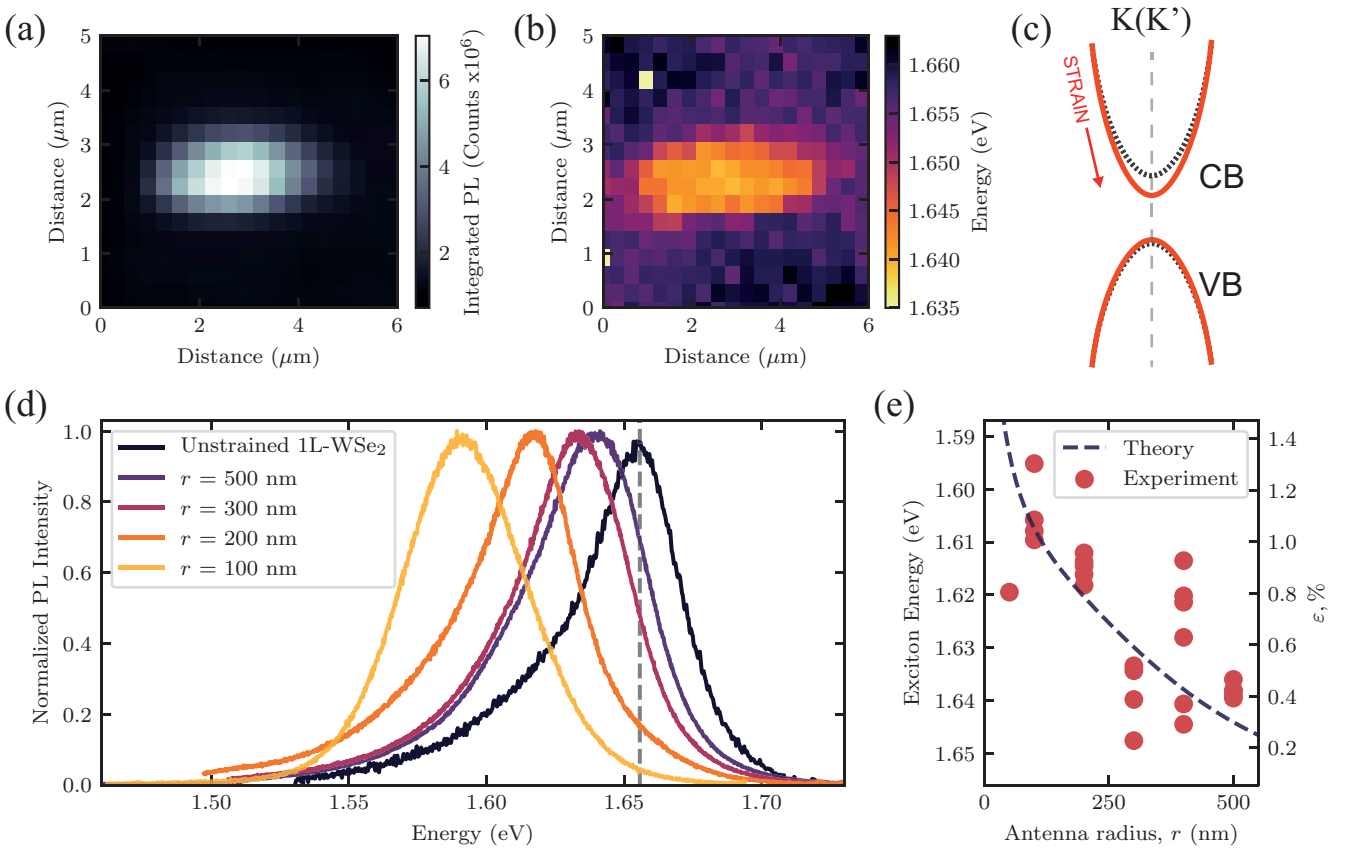

FIG. 2. (a) PL intensity map for 1L-WSe_2 placed on a GaP nano-antenna with $r = 300$ nm measured using a micro-PL set-up. (b) The same map as in (a), but showing the exciton peak energy distribution. (c) Schematics showing how the band-structure around the K valley in 1L-WSe_2 is modified under tensile strain (red). The band-structure for the unstrained 1L-WSe_2 is shown in black. (d) Normalized PL spectra for 1L-WSe_2 placed on top of nano-antennas with different radii r. The red-shift observed for decreasing r corresponds to increasing strain in WSe_2. (e) Symbols show PL peak positions for 1L-WSe_2 placed on nano-antennas with different r and corresponding uniaxial strain deduced using the experimental gauge factor from Ref.[57]. Dashed line shows the strain values calculated using our theoretical model.

antenna radius is reduced, comparable to the estimate from our theoretical model shown with the dashed line (see also Supplementary Fig.S1). There is a variation in the peak position measured on different pillars. This effect can be attributed to the non-uniform coverage of the antenna surface by the monolayer and from the local disorder introduced in the WSe_2 layer, for instance from wrinkles, folding, contamination, etc.

Direct bandgap transition in 2L-WSe_2 As schematically shown in Fig.3a, using a single particle picture, contrary to the monolayer case, a WSe_2 bilayer is an indirect bandgap semiconductor. It exhibits two main recombination pathways at room temperature, a momentum direct (higher energy) and indirect (lower energy) transition, respectively involving the K and Q points of the conduction band [18]. For unstrained 2L-WSe_2 (black dashed line) the lowest energy transition is the phonon-assisted recombination between the conduction band minimum at the Q point and the valence band maximum at the K point. In analogy with the monolayer case, under tensile strain (coloured lines in Fig.3a) the conduction band minimum at the K and Q point exhibit a reduction in their energy [19], with a stronger shift expected for the K valley. This difference in the tuning of the valleys has been shown to lead to the transition from the indirect to direct bandgap in strained 2L-WSe_2 [4, 67]. Note, that in the exciton picture, the behaviour described above will translate in the corresponding energy shifts of the momentum-bright K-K exciton and the momentum-dark Q-K exciton.

Fig.3b shows a room temperature PL spectrum for the unstrained 2L-WSe_2 placed on a flat GaP substrate. In contrast to what found for the monolayer, the bilayer exhibits a broad spectrum composed of two peaks, attributed to the momentum indirect $E_{\mathrm{Indirect}} = 1.55$ eV and momentum direct $E_{\mathrm{Direct}} = 1.63$ eV exciton transi-

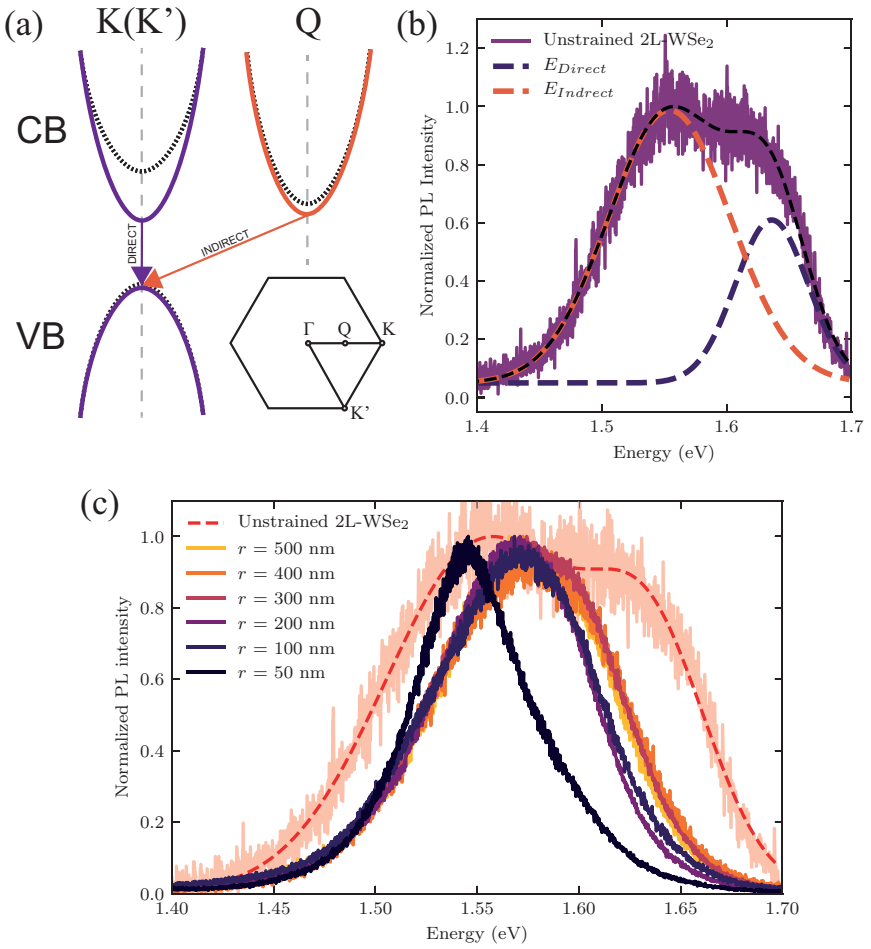

FIG. 3. (a) Schematic of the band structure modification in 2L-WSe_2 under tensile strain. The black dashed line shows the case of the unstrained 2L-WSe_2, where the lowest energy radiative recombination occurs as a result of the momentum-indirect $Q \rightarrow K$ transition. Purple (orange) lines show the modification of the $K(Q)$ valley energies under tensile strain. Arrows show momentum-direct (purple) and indirect (orange) transitions giving rise to PL. (b) PL spectrum of unstrained 2L-WSe_2 placed on a planar GaP substrate. Fitting reveals individual PL peaks associated with the indirect ($Q \rightarrow K$, E_{Indirect}, orange) and the direct ($K \rightarrow K$, E_{Direct}, purple) transitions. (c) Normalized PL spectra measured for 2L-WSe_2 on top of GaP nano-antennas with different radii and deposited on planar GaP substrate (dashed line).

tions [18, 68]. The corresponding individual peaks obtained from the fitting of the PL spectrum are shown with dashed lines in Fig.3b.

In analogy with the analysis carried out for WSe_2 monolayers, we collected the PL emission of the strained bilayer placed on top of the nano-antennas with different radii. The normalized PL spectra measured for the nano-antennas of different radii are shown in Fig.3c. For the strained WSe_2 bilayer, the presence of two transitions leads to a less evident strain-induced shift of the PL spectra. However, by comparing the spectral shape to that of the unstrained case we observe that, as the nano-antenna radius is reduced, the higher energy side of the spectrum shows a consistent shift to lower energies, following an abrupt change of the PL spectrum from that on the flat GaP (dashed red line) to the spectrum measured on a pillar with $r = 500$ nm (yellow). The shift is accompanied with a reduction of the linewidth related to the reduction of the exciton-phonon coupling in WSe_2 under strain [57]. We attribute the red-shift under increasing tensile strain to the reduction in energy of the $K \rightarrow K$ transition, as we observed for the monolayer case. Moreover, the PL lineshape exhibits a further abrupt change when the 2L-WSe_2 is deposited on top of a GaP dimer nano-antenna with $r = 50$ nm. This spectral shape and peak position resemble those reported in Ref.[4, 67] where they were attributed to a transition to the direct bandgap, occurring due to the red-shift of the high-energy peak at E_{Direct} (see also Supplementary Note III). Our theoretical model predicts strain values $> 3\%$ for 2L-WSe_2 placed on the nano-antennas with $r = 50$ nm (see Supplementary Fig.S1). This value is compara-

ble with the reported threshold for the direct bandgap transition observed in WSe_2 bilayers [67].

Note, that for the pillars of the same radius, a higher strain is introduced in the bilayer compared with a monolayer, due to the larger rigidity and larger mass of the former. Thus, a stronger bandgap tuning is observed in a bilayer. A similar effect has been reported in suspended 1L and 2L-MoS_2 under the strain introduced by an AFM probe [28].

Exciton confinement in the strain-induced potential Controlled nano-scale deformations observed in Fig.1-3 allow the control of exciton motion in 2D semiconductors by means of band structure modification [32, 33]. For WSe_2, the application of tensile strain results in the increase of the valence band edge energy and reduction of the conduction band edge energy at the K point. This effect leads to so-called exciton funnelling [1, 32], where a strain gradient directs the excitonic population towards the strain-induced potential well. This effect has been proposed to play a role in the population of the single photon emitting centres in WSe_2 at cryogenic temperatures [34, 35]. In order to elucidate the role of the confinement produced by the strain, we probed the spatial dependence of the PL emission of 2L-WSe_2. The experiments are carried out at a cryogenic temperature of 4 K where the effect of the strain-induced confinement is most pronounced.

From our strain topography model, it is possible to calculate the strain-induced potential for the case of the dimer structures (see Supplementary Fig.S2). We find that the strain-induced potential wells are located at the nano-pillars edges, where the tensile strain is maximized [1, 32]. When strain becomes compressive, i.e. where the layer touches the substrate, we observe the presence of potential barriers due to the opposite shift of the band edges, leading to an increase of the bandgap energy. Fig.4a shows the profile of the strained 2L-WSe_2 (dashed line) on top of a dimer nano-antenna with $r = 500$ nm (red squares). The TMD profile shown in the top panel is calculated for a cross section along the $x-$axis (as defined in Fig.1e), where $x = 0$ is the centre of the dimer gap. We correlate the local deformation with the changes in the energy of the conduction band minimum ($V_{\rm cb}$), calculated numerically for the K valley (see the bottom panel in Fig.4a and Supplementary Note I for details). The minima of $V_{\rm cb}$ are localized at the nano-pillar edges, resulting in a confinement potential wells (shaded areas). For WSe_2 the valence band maximum, $V_{\rm vb}$, exhibits an increase (decrease) in case of tensile (compressive) strain, also resulting in a confinement for holes, although this effect is weaker compared to conduction band electrons. In such a potential landscape, the exciton population will accumulate in the potential wells at the nano-pillar edges.

Fig.4b shows a reference PL spectrum of 2L-WSe_2 collected at T =4 K on the planar GaP (black) and on a dimer nano-antenna with $r = 500$ nm (orange). The low temperature PL of 2L-WSe_2 is dominated by the low energy broad band between 1.5 and 1.6 eV, relatively weakly dependent on the strain induced by the dimer. Overall the spectrum is rather complicated due to the non-trivial combination of PL from bright and dark states, phonon replicas [69] and emission of various localized states [70]. The only part of this broad band that consistently shows dependence on the strain induced by the pillars is the lower side of the spectrum between 1.5 and 1.55 eV, which exhibits higher intensity in the strained WSe_2. One of the reasons for such behaviour could be that the PL in the range 1.55-1.6 eV may originate from the transitions involving the Q valley in the conduction band [69], which is weakly sensitive to the strain. On the other hand, we may conclude that the PL in the spectral range of 1.5 to 1.55 eV may arise from the localized exciton states, with the energies following the overall reduction in the direct bandgap by about 45 meV (see details below), or perhaps the optical transitions involving the K valley in the conduction band. However, the complete understanding of this behaviour requires elaborate theory for the optical transitions in bilayer WSe_2 and is beyond the scope of this work.

Despite the very low PL intensity, as expected at low T in WSe_2, we are still able to observe the momentum-direct $K \rightarrow K$ exciton transition for the unstrained WSe_2 on the planar GaP at 1.7 eV (inset Fig.4b). As expected for the direct transition, in the strained WSe_2 placed on the nano-antenna, the corresponding exciton peak is observed approximately 45 meV lower at 1.655 eV (denoted X). From this energy red-shift we estimate a tensile strain value of $\approx 1\%$, consistent with our theoretical model predictions. As we show in Supplementary Note IV, we observe a similar red-shift in the cryogenic PL of the strained 1L-WSe_2 exciton, also in agreement with our model.

Fig.4c shows a one-dimensional hyper-spectral PL image of 2L-WSe_2 placed on top of four GaP nano-antennas having $r = 500$ nm and the gap size varying between 100 and 150 nm from left to right. The PL image is measured by scanning the collection and excitation spot along the nano-antenna x-axis (see Fig.1e for the axis definition), while on the vertical axis of the figure we report the spectral distribution of the collected PL emission. The increased PL intensity corresponds to the enhanced 2L-WSe_2 PL on top of the dimer nano-antennas, with a negligible signal collected on the flat GaP (dark areas in between).

In the right panel of Fig.4c we zoom in on the direct exciton PL emission in the strained WSe_2 at around 1.655 eV. The exciton PL intensity exhibits a clear localization into two spatially separated maxima. Fig.4d shows the integrated intensity of the exciton PL (in black) clearly highlighting this behaviour. Such two-peaked distribution is also reproduced to some degree for the lowest part of the PL spectrum below ≈ 1.52 eV. This is a conse-

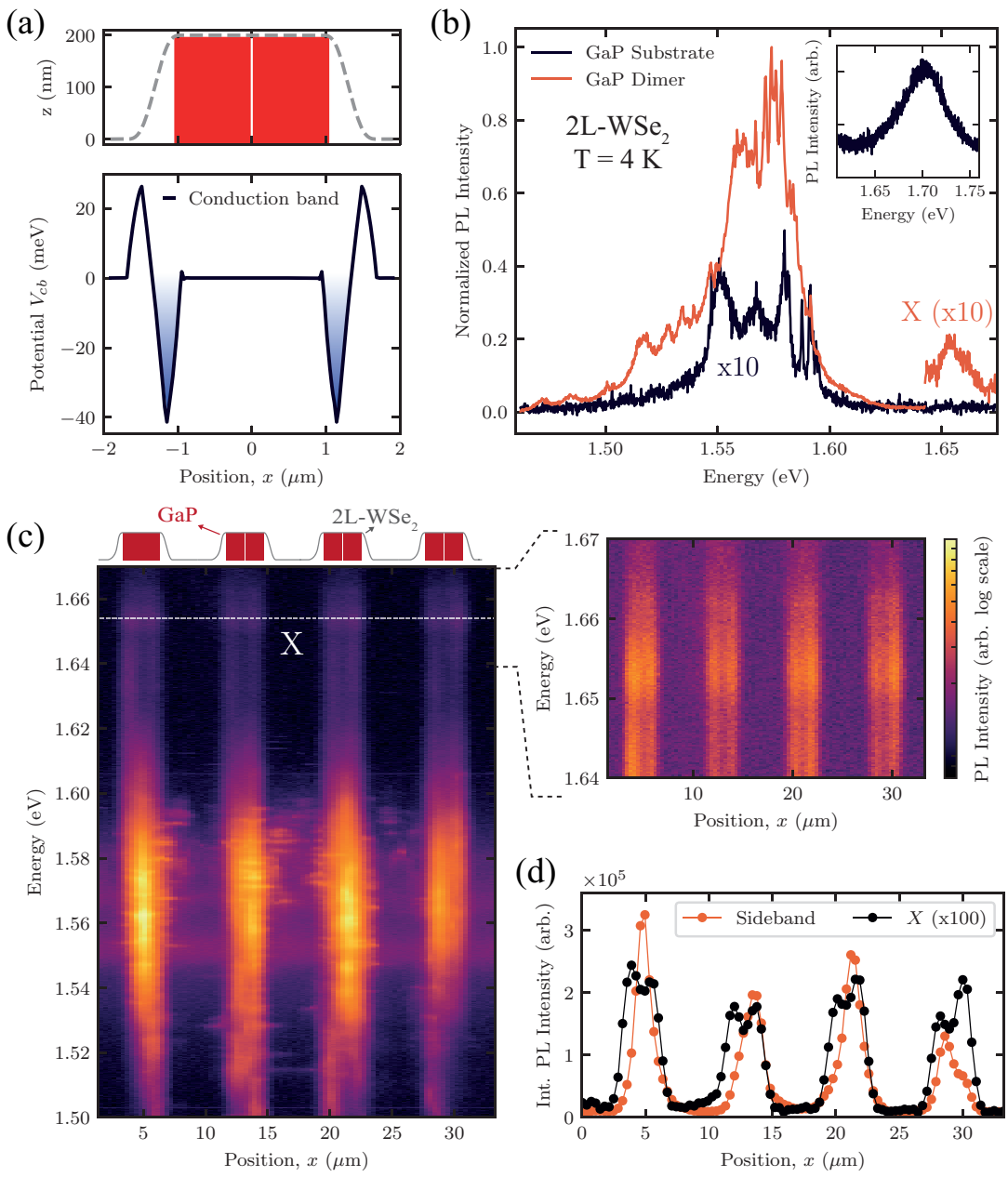

FIG. 4. (a) Top panel: cross-section along the x-axis (defined as in Fig.1e) of the profile for the 2L-WSe_2 (dashed line) on top of a dimer nano-antenna (in red, h = 200 nm, r = 500 nm). Bottom panel: strain-induced potential (V_{cb}) calculated for the K valley in the conduction band as a function of x. (b) 2L-WSe_2 PL spectra at T=4 K, collected on top of the dimer nano-antenna (r = 500 nm, orange) and on the planar GaP substrate (black). The spectrum for the nano-antenna is divided by a factor corresponding to its maximum intensity (i.e. normalized). The spectrum measured for the planar GaP is divided by the same factor and multiplied by ten. A part of the orange spectrum around 1.65 eV corresponding to the intralayer exciton PL is further multiplied by 10 and denoted X. Inset shows intralayer exciton PL measured for 2L-WSe_2 placed on the planar GaP substrate exhibiting a maximum around 1.7 eV. (c) Hyper-spectral image showing PL for 2L-WSe_2 deposited on top of four dimer nano-antennas (r = 500 nm) separated by $\approx$ 10 μm (schematically shown at the top of the panel). As shown in the zoomed-in image, the spatial distribution of the intralayer exciton PL shows a clear localization in two spatially separated PL maxima, as predicted by the calculated potential presented in Fig.4a. (d) Integrated PL intensity as a function of x. The data in black is for the intralayer exciton with integration limits 1.65-1.66 eV (the PL intensity is multiplied by 100), and in orange for the broad PL band with integration limits 1.56-1.58 eV.

quence of the sensitivity of this part of the spectrum to the induced strain as observed in Fig.4b. We conclude that for the two types of states, exciton funnelling to the strain-induced potential minima is significant.

As seen both in Fig.4c and d, such two-peaked distribution is not replicated clearly for the broad band between 1.55 and 1.6 eV, which is consistent with a weak sensitivity of the involved electronic states to the strain observed in Fig.4b.

DISCUSSION

In summary, we have demonstrated strain-tuning of the electronic band structure in 2D semiconductor WSe_2 by placing the atomic mono- and bilayers on pre-patterned dielectric nano-antennas. Because of the efficient coupling with the optical mode confined at the surface of the nano-antenna, the PL of the strained WSe_2 is enhanced. It can thus be clearly detected with negligible contribution from the PL of the unstrained material, that would normally mask the effect of strain, for example, in the case of the pillars made of SiO_2 or polymers, which were employed previously to induce strain [31, 35]. We therefore can clearly deduce the amount of induced strain from the red-shift in WSe_2 PL spectra at room temperature in agreement with our theory. Moreover, we observe excitons confined into strain-induced potential wells at cryogenic temperature, the presence of which is also predicted by our theoretical model. This effect provides evidence for the exciton funnelling in strained 2D semiconductors.

The results presented in this work open the way for the use of strain as an additional degree of freedom in engineering of the light-matter interaction in 2D materials, and could find applications for studying 2D excitons in confined potentials, relevant for positioning of strain-induced WSe_2 quantum emitters[34, 35], as well as for Bose-Einstein condensation of interlayer excitons in TMDs heterostructures[71, 72].

Additionally, our continuum-mechanical theoretical approach can be expanded to describe the strain distribution and resulting distortion potential for 2D TMDs coupled to a broad range of nano-structures including plasmonic nano-antennas. This opens the way for designing optically active nano-photonic platforms interfaced with strained 2D materials and their heterostructures, with prospects in photodetection, light emission and photovoltaic applications.

Methods

Sample fabrication The GaP nano-antennas are fabricated with a top-down lithography process, as described in Ref.[56]. The monolayers and bilayers of WSe_2 were mechanically exfoliated from commercially available bulk crystal (HQGraphene) and the layer thickness identified via a PL imaging technique[62]. The 2D layers are transferred on top of the GaP nano-antennas in a home-built transfer setup, with an all-dry transfer technique[73].

Optical spectroscopy The PL image used in Fig.1d is obtained in a commercial bright-field microscope (LV150N Nikon), with the technique described in Ref.[62], where the white light source is used both to image the TMD layers and to excite its PL emission. A 550 nm short-pass filter is placed in the illumination beam path to remove the low energy side of the white light emission spectrum. A high numerical aperture objective (Nikon x100 NA=0.9) is used to direct the light on the sample and for collecting the reflected and emitted light. In the collection path a 600 nm long-pass filter rejects the white light source, while the PL image from the TMD layer is detected with a microscope camera (DS-Vi1, Nikon). Room temperature optical spectroscopy is performed in a home built micro-PL setup in back reflection geometry. A diode laser is used as the excitation source and directed into an infinity corrected objective (Mitutoyo 100x NA=0.7). The sample is placed on a motorized stage (STANDA-8MTF) which allows the automated mapping of the sample surface. The emitted light is collected by the same objective and coupled to a spectrometer (Princeton Instruments SP2750) with a high-sensitivity liquid nitrogen cooled charge-coupled device (Princeton Instruments PyLoN). For optical spectroscopy at cryogenic temperature, the sample is placed into a microscope stick (attocube systems AG) with a cage structure and a window for optical access. The sample is placed onto piezoelectric nano-positioners (attocube ANP101 models). The cage structure is fitted into an aluminium tube and held under high-vacuum. The tube is then inserted in a liquid helium bath cryostat and an optical breadboard with a micro-PL setup is placed on top of the tube to carry out the optical analysis. The light emitted by the sample is coupled to a single mode optical fibre and detected in the same spectrometer/CCD system employed for the room temperature spectroscopy.

Acknowledgement
L. S. and A. I. T. thank the financial support of the European Graphene Flagship Project under grant agreements 785219, and EPSRC grant EP/S030751/1. L. S., A. I. T., M. B. and G. B. thank the European Union's Horizon 2020 research and innovation programme under ITN Spin-NANO Marie Sklodowska-Curie grant agreement no. 676108. P. G. Z. and A. I. T. thank the European Union's Horizon 2020 research and innovation programme under ITN 4PHOTON Marie Sklodowska-Curie grant agreement no. 721394. A. G. and A. I. T. acknowledge funding by EPSRC grant EP/P026850/1. J. C., S. M., S. A. M., and R. S. acknowledge funding by EPSRC (EP/P033369 and EP/M013812). S. A. M. acknowledges the Lee-Lucas Chair in Physics and the Solar Energies go Hybrid (SolTech) programme.

Author contributions

L. S., A. I. T., S. A. M., R. S. conceived the idea of the experiment. L. S. and P. G. Z. fabricated WSe_2 layers and transferred them on the GaP nano-antennas. L. S., P. G. Z. and A. G. carried out microscopy and optical spectroscopy measurements on WSe_2. J. C. fabricated GaP nano-antennas. S. M., J. C. and R. S. designed GaP nano-antennas. L. S., P. G. Z., A. G. and A. I. T. analysed optical spectroscopy data. M. B. and G. B. developed the theory and carried out simulations for strained WSe_2. G. B., S. A. M., R. S. and A. I. T. managed various aspects of the project. L. S., M. B. and A. I. T. wrote the manuscript with contributions from all co-authors. A. I. T. oversaw the whole project.

* l.sortino@sheffield.ac.uk
† a.tartakovskii@sheffield.ac.uk

[1] Y. Sun, S. E. Thompson, and T. Nishida, *Springer US* (Springer US, Boston, MA, 2010) p. 350.
[2] C. Lee, X. Wei, J. W. Kysar, and J. Hone, Science (80-.). **321**, 385 (2008).
[3] F. Guinea, M. I. Katsnelson, and A. K. Geim, Nat. Phys. **6**, 30 (2010).
[4] K.-A. N. Duerloo, M. T. Ong, and E. J. Reed, J. Phys. Chem. Lett. **3**, 2871 (2012).
[5] W. Wu, L. Wang, Y. Li, F. Zhang, L. Lin, S. Niu, D. Chenet, X. Zhang, Y. Hao, T. F. Heinz, J. Hone, and Z. L. Wang, Nature **514**, 470 (2014).
[6] R. Roldán, A. Castellanos-Gomez, E. Cappelluti, and F. Guinea, J. Phys. Condens. Matter **27**, 313201 (2015).
[7] B. Amorim, A. Cortijo, F. De Juan, A. G. Grushin, F. Guinea, A. Gutiérrez-Rubio, H. Ochoa, V. Parente, R. Roldán, P. San-Jose, J. Schiefele, M. Sturla, and M. A. Vozmediano, Phys. Rep. **617**, 1 (2015).
[8] Z. Dai, L. Liu, and Z. Zhang, Adv. Mater. **1805417**, 1805417 (2019), arXiv:0507464v2 [arXiv:astro-ph].
[9] D. Akinwande, N. Petrone, and J. Hone, Nat. Commun. **5**, 5678 (2014).
[10] T. Mueller and E. Malic, npj 2D Mater. Appl. **2**, 29 (2018).
[11] S. Manzeli, D. Ovchinnikov, D. Pasquier, O. V. Yazyev, and A. Kis, Nat. Rev. Mater. **2** (2017), 10.1038/natrevmats.2017.33.
[12] K. F. Mak, C. Lee, J. Hone, J. Shan, and T. F. Heinz, Phys. Rev. Lett. **105**, 136805 (2010).
[13] A. Splendiani, L. Sun, Y. Zhang, T. Li, J. Kim, C.-Y. Chim, G. Galli, and F. Wang, Nano Lett. **10**, 1271 (2010).
[14] K. He, N. Kumar, L. Zhao, Z. Wang, K. F. Mak, H. Zhao, and J. Shan, Phys. Rev. Lett. **113**, 026803 (2014), arXiv:1406.3095.
[15] G. Wang, A. Chernikov, M. M. Glazov, T. F. Heinz, X. Marie, T. Amand, and B. Urbaszek, Rev. Mod. Phys. **90**, 021001 (2018).
[16] X. Xu, W. Yao, D. Xiao, and T. F. Heinz, Nat. Phys. **10**, 343 (2014).
[17] S. Bertolazzi, J. Brivio, and A. Kis, ACS Nano **5**, 9703 (2011).
[18] W. S. Yun, S. W. Han, S. C. Hong, I. G. Kim, and J. D. Lee, Phys. Rev. B **85**, 033305 (2012).
[19] P. Johari and V. B. Shenoy, ACS Nano **6**, 5449 (2012).
[20] C.-H. Chang, X. Fan, S.-H. Lin, and J.-L. Kuo, Phys. Rev. B **88**, 195420 (2013).
[21] D. M. Guzman and A. Strachan, J. Appl. Phys. **115**, 243701 (2014), arXiv:1312.1275.
[22] H. J. Conley, B. Wang, J. I. Ziegler, R. F. Haglund, S. T. Pantelides, and K. I. Bolotin, Nano Lett. **13**, 3626 (2013).
[23] A. Castellanos-Gomez, R. Roldán, E. Cappelluti, M. Buscema, F. Guinea, H. S. J. van der Zant, and G. A. Steele, Nano Lett. **13**, 5361 (2013).
[24] M. Feierabend, A. Morlet, G. Berghäuser, and E. Malic, Phys. Rev. B **96**, 045425 (2017).
[25] O. B. Aslan, M. Deng, and T. F. Heinz, Phys. Rev. B **98**, 115308 (2018).
[26] R. Schmidt, I. Niehues, R. Schneider, M. Drüppel, T. Deilmann, M. Rohlfing, S. M. de Vasconcellos, A. Castellanos-Gomez, and R. Bratschitsch, 2D Mater. **3**, 021011 (2016).
[27] T. Liu, S. Liu, K.-H. Tu, H. Schmidt, L. Chu, D. Xiang, J. Martin, G. Eda, C. A. Ross, and S. Garaj, Nat. Nanotechnol. **1**, 1 (2019).
[28] S. Manzeli, A. Allain, A. Ghadimi, and A. Kis, Nano Lett. **15**, 5330 (2015).
[29] A. De Sanctis, I. Amit, S. P. Hepplestone, M. F. Craciun, and S. Russo, Nat. Commun. **9**, 1652 (2018).
[30] B. G. Shin, G. H. Han, S. J. Yun, H. M. Oh, J. J. Bae, Y. J. Song, C.-Y. Park, and Y. H. Lee, Adv. Mater. **28**, 9378 (2016).
[31] H. Li, A. W. Contryman, X. Qian, S. M. Ardakani, Y. Gong, X. Wang, J. M. Weisse, C. H. Lee, J. Zhao, P. M. Ajayan, J. Li, H. C. Manoharan, and X. Zheng, Nat. Commun. **6**, 7381 (2015).
[32] J. Feng, X. Qian, C.-W. Huang, and J. Li, Nat. Photonics **6**, 866 (2012).
[33] P. San-Jose, V. Parente, F. Guinea, R. Roldán, and E. Prada, Phys. Rev. X **6**, 031046 (2016).
[34] A. Branny, S. Kumar, R. Proux, and B. D. Gerardot, Nat. Commun. **8**, 15053 (2017).
[35] C. Palacios-Berraquero, D. M. Kara, A. R.-P. Montblanch, M. Barbone, P. Latawiec, D. Yoon, A. K. Ott, M. Loncar, A. C. Ferrari, and M. Atatüre, Nat. Commun. **8**, 15093 (2017).
[36] P. Gant, P. Huang, D. Pérez de Lara, D. Guo, R. Frisenda, and A. Castellanos-Gomez, Mater. Today **27**, 8 (2019).
[37] R.-J. Shiue, D. K. Efetov, G. Grosso, C. Peng, K. C. Fong, and D. Englund, Nanophotonics **6**, 1329 (2017).
[38] J. A. Schuller, E. S. Barnard, W. Cai, Y. C. Jun, J. S. White, and M. L. Brongersma, Nat. Mater. **9**, 193 (2010).
[39] L. Novotny and N. van Hulst, Nat. Photonics **5**, 83 (2011).
[40] A. F. Koenderink, ACS Photonics **4**, 710 (2017).
[41] D. G. Baranov, M. Wersäll, J. Cuadra, T. J. Antosiewicz, and T. Shegai, ACS Photonics **5**, 24 (2018).
[5] L. Sortino, P. G. Zotev, S. Mignuzzi, J. Cambiasso, D. Schmidt, A. Genco, M. Aßmann, M. Bayer, S. A. Maier, R. Sapienza, and A. I. Tartakovskii, Nat. Commun. **10**, 5119 (2019).
[43] G. M. Akselrod, T. Ming, C. Argyropoulos, T. B. Hoang, Y. Lin, X. Ling, D. R. Smith, J. Kong, and M. H. Mikkelsen, Nano Lett. **15**, 3578 (2015).
[44] Z. Wang, Z. Dong, Y. Gu, Y.-H. Chang, L. Zhang, L.-J. Li, W. Zhao, G. Eda, W. Zhang, G. Grinblat, S. A.

Maier, J. K. W. Yang, C.-W. Qiu, and A. T. S. Wee, Nat. Commun. **7**, 11283 (2016).
[45] S. A. Maier, *Plasmonics: Fundamentals and Applications* (Springer US, New York, NY, 2007).
[46] V. Giannini, A. I. Fernandez-Dominguez, S. C. Heck, and S. A. Maier, Chem. Rev. **111**, 3888 (2011).
[47] J. T. Hugall, A. Singh, and N. F. Van Hulst, ACS Photonics **5**, 43 (2018).
[48] A. I. Kuznetsov, A. E. Miroshnichenko, M. L. Brongersma, Y. S. Kivshar, and B. Luk'yanchuk, Science (80-.). **354**, aag2472 (2016).
[49] J. Cambiasso, M. König, E. Cortés, S. Schlücker, and S. A. Maier, ACS Photonics **5**, 1546 (2018).
[50] M. Caldarola, P. Albella, E. Cortés, M. Rahmani, T. Roschuk, G. Grinblat, R. F. Oulton, A. V. Bragas, and S. A. Maier, Nat. Commun. **6**, 7915 (2015).
[51] A. I. Kuznetsov, A. E. Miroshnichenko, Y. H. Fu, J. Zhang, and B. Luk'yanchuk, Sci. Rep. **2**, 492 (2012), arXiv:1205.1610.
[52] A. F. Cihan, A. G. Curto, S. Raza, P. G. Kik, and M. L. Brongersma, Nat. Photonics **12**, 284 (2018).
[53] Y. Y. Hui, X. Liu, W. Jie, N. Y. Chan, J. Hao, Y.-T. Hsu, L.-J. Li, W. Guo, and S. P. Lau, ACS Nano **7**, 7126 (2013).
[54] G. Plechinger, A. Castellanos-Gomez, M. Buscema, H. S. J. van der Zant, G. A. Steele, A. Kuc, T. Heine, C. Schüller, and T. Korn, 2D Mater. **2**, 015006 (2015).
[55] G. H. Ahn, M. Amani, H. Rasool, D. H. Lien, J. P. Mastandrea, J. W. Ager, M. Dubey, D. C. Chrzan, A. M. Minor, and A. Javey, Nat. Commun. **8**, 1 (2017).
[56] J. Cambiasso, G. Grinblat, Y. Li, A. Rakovich, E. Cortés, and S. A. Maier, Nano Lett. **17**, 1219 (2017).
[57] I. Niehues, R. Schmidt, M. Drüppel, P. Marauhn, D. Christiansen, M. Selig, G. Berghäuser, D. Wigger, R. Schneider, L. Braasch, R. Koch, A. Castellanos-Gomez, T. Kuhn, A. Knorr, E. Malic, M. Rohlfing, S. Michaelis de Vasconcellos, and R. Bratschitsch, Nano Lett. **18**, 1751 (2018).
[1] M. Brooks and G. Burkard, Phys. Rev. B **97**, 195454 (2018).
[2] L. Landau, E. Lifshitz, A. Kosevich, and L. Pitaevski, *Theory of Elasticity* (Elsevier, 1986).
[60] T. Cai, J.-H. Kim, Z. Yang, S. Dutta, S. Aghaeimeibodi, and E. Waks, ACS Photonics **5**, 3466 (2018), arXiv:1803.09358.
[61] Y. Luo, G. D. Shepard, J. V. Ardelean, D. A. Rhodes, B. Kim, K. Barmak, J. C. Hone, and S. Strauf, Nat. Nanotechnol. **13**, 1137 (2018).
[62] E. M. Alexeev, A. Catanzaro, O. V. Skrypka, P. K. Nayak, S. Ahn, S. Pak, J. Lee, J. I. Sohn, K. S. Novoselov, H. S. Shin, and A. I. Tartakovskii, Nano Lett. **17**, 5342 (2017).
[63] A. Kormányos, G. Burkard, M. Gmitra, J. Fabian, V. Zólyomi, N. D. Drummond, and V. Fal'ko, 2D Mater. **2**, 022001 (2015).
[64] S. Heeg, R. Fernandez-Garcia, A. Oikonomou, F. Schedin, R. Narula, S. A. Maier, A. Vijayaraghavan, and S. Reich, Nano Lett. **13**, 301 (2013).
[65] S. Heeg, A. Oikonomou, R. F. Garcia, S. A. Maier, A. Vijayaraghavan, and S. Reich, Phys. status solidi - Rapid Res. Lett. **7**, 1067 (2013).
[4] S. B. Desai, G. Seol, J. S. Kang, H. Fang, C. Battaglia, R. Kapadia, J. W. Ager, J. Guo, and A. Javey, Nano Lett. **14**, 4592 (2014).
[67] W. Wu, J. Wang, P. Ercius, N. C. Wright, D. M. Leppert-Simenauer, R. A. Burke, M. Dubey, A. M. Dogare, and M. T. Pettes, Nano Lett. **18**, 2351 (2018).
[68] W. Zhao, R. M. Ribeiro, M. Toh, A. Carvalho, C. Kloc, A. H. Castro Neto, and G. Eda, Nano Lett. **13**, 5627 (2013).
[69] J. Lindlau, M. Selig, A. Neumann, L. Colombier, J. Förste, V. Funk, M. Förg, J. Kim, G. Berghäuser, T. Taniguchi, K. Watanabe, F. Wang, E. Malic, and A. Högele, Nat. Commun. **9**, 2586 (2018).
[70] S. Kumar, A. Kaczmarczyk, and B. D. Gerardot, Nano Lett. **15**, 7567 (2015).
[71] P. Rivera, H. Yu, K. L. Seyler, N. P. Wilson, W. Yao, and X. Xu, Nat. Nanotechnol. **13**, 1004 (2018).
[72] Z. Wang, D. A. Rhodes, K. Watanabe, T. Taniguchi, J. C. Hone, J. Shan, and K. F. Mak, Nature **574**, 76 (2019).
[73] A. Castellanos-Gomez, M. Buscema, R. Molenaar, V. Singh, L. Janssen, H. S. J. van der Zant, and G. A. Steele, 2D Mater. **1**, 011002 (2014).

SUPPLEMENTARY NOTE I: STRAIN TOPOGRAPHY THEORETICAL MODELLING

The strain topography of stretched transition metal dichalcogenides (TMD) layers is achieved by modelling the out-of-plane displacement relative to the underlying substrate. We applied a continuum-mechanical plate-theory approach, as introduced in Ref.[1], with the following reduced form of the Föppl-von Kármán equations, valid for such passively strained low-dimensional systems [2]:

$$D\Delta^2\zeta - P = 0 \tag{1}$$

where P is the pressure the atomic layer experiences, ζ is the function that describes the height profile of the layer [1], Δ^2 is the biharmonic operator, given by the square of the Laplacian Δ, and D is the flexural rigidity of the TMD layer defined as:

$$D = \frac{Eh^3}{12(1-\sigma^2)} \tag{2}$$

here E is the Young's modulus, σ is the Poissons ratio and h is the TMD layer thickness.

To model the WSe_2 strain topography above the dimer structure, we found a solution to Eq.1. The model of pressure [1] adopted here, consistent with the microscopy measurements, is the plate model (P = 0) with boundary conditions:

$$\zeta_{\mathrm{P}=0}(r) = H \tag{3}$$
$$\zeta_{\mathrm{P}=0}(r_{\mathrm{T}}) = 0 \tag{4}$$
$$\partial_\rho \zeta_{\mathrm{P}=0}|_{\mathrm{r},\mathrm{r_T}} = 0 \tag{5}$$

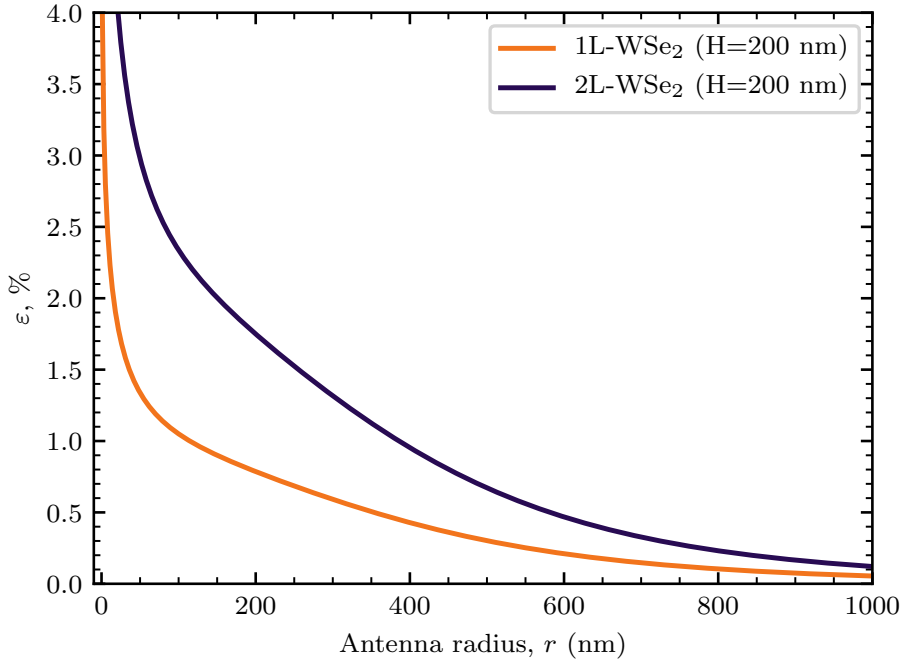

SUPPLEMENTARY FIGURE .1. Uniaxial tensile strain values as a function of the nano-pillar radius, calculated at the topmost edge of the dimer nano-antenna (H = 200 nm) for both single and double layer WSe_2.

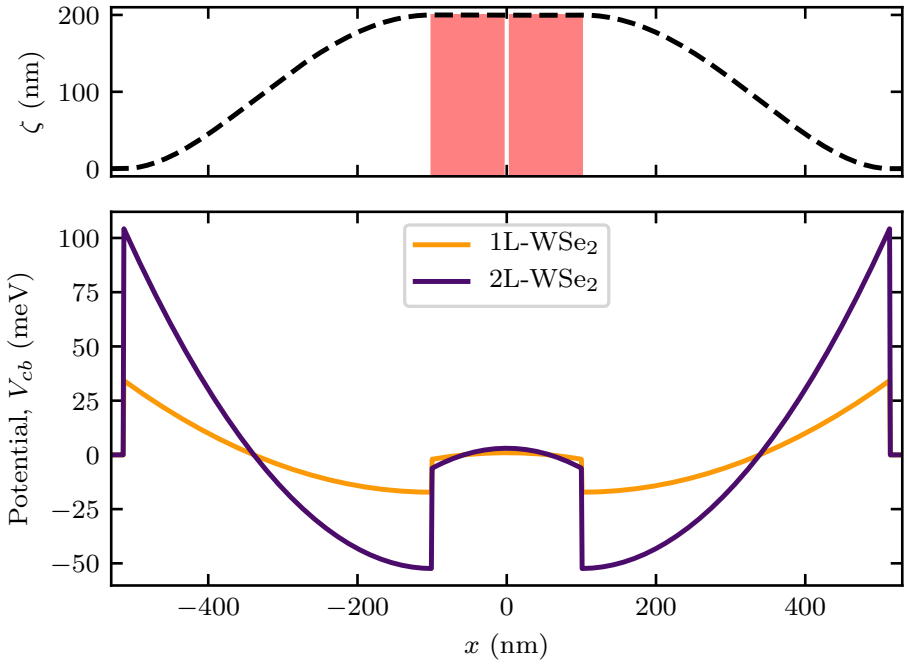

SUPPLEMENTARY FIGURE .2. Top panel: Height field profile (black dashed line) for a dimer with $H = 200$ nm and $r = 50$ nm, schematically shown in red. Bottom panel: conduction band potential minimum (V_{cb}), calculated for the K(K') point of the Brillouin zone, for both single (1L) and double (2L) layer WSe_2, relative to the height field profile shown in the top panel. The compressive (tensile) strain region is correlated to an increase (decrease) of the potential value.

where H is the height of the dimer antenna, r is the nano-pillar radius and r_{T} is the tenting radius, the distance between the antenna pillars and the point where the WSe_2 layer meets the substrate. We obtain the following analytical solution for the height field, relative to a single pillar, in rotational symmetry:

$$\zeta_{\mathrm{P}=0}(\rho) = \frac{H}{(r_{\mathrm{T}}^2 - r^2)^{\,2} - 4r_{\mathrm{T}}^2 r^2 \ln^2\left[\frac{r_{\mathrm{T}}}{r}\right]} \left\{ 2r_{\mathrm{T}}^2 \ln[r_{\mathrm{T}}] \left(r^2 + 2r^2 \ln\left[\frac{r}{r_{\mathrm{T}}}\right] - \rho^2 \right) \right. \tag{6}$$

$$+ \left(\rho^2 - r_{\mathrm{T}}^2\right) \left(r^2 + 2r^2 \ln[r] - r_{\mathrm{T}}^2 \right) \tag{7}$$

$$\left. +2\ln[\rho] \left(\rho^2 \left(r_{\mathrm{T}}^2 - r^2 \right) + 2r_{\mathrm{T}}^2 r^2 \ln\left[\frac{r_{\mathrm{T}}}{r}\right] \right) \right\} \tag{8}$$

Taking this approximation as a starting point, we obtain a numerically averaged height field over the dimer geometry by taking values of r_{T} from microscopy measurements, and interpolation in the gap region where the rational symmetry of the approximate model is violated. From a satisfactory model of the height field, the strain component responsible for the band gap renormalization is given by the trace of the strain tensor $\varepsilon_{\mathrm{ij}}$, given as[3]:

$$\mathcal{T} = Tr[\varepsilon_{\mathrm{ij}}] = \frac{(2\sigma - 1)h}{1 - \sigma} \Delta\zeta \tag{9}$$

We resolved a relationship between the tensile strain maximum and the nano-pillar radius. Fig.S.1 shows the calculated strain values at the topmost edge of a nano-antenna ($H = 200$ nm), as a function of the nano-pillar radius. For both 1L and 2L-WSe_2 we observe an increased strain value as r decreases, with a stronger magnitude for the bilayer. This trend can be explained as the assumed model approaches a deflection of a Dirac-delta like deformation, when $r \to 0$, giving an undefined pole in the strain value. An increased strain in bilayers is directly related to its larger rigidity (Eq.2).

After defining a strain topography, it is possible to calculate a strain-induced deformation potential in the WSe_2 band structure, following a tight-binding approach[1, 3], as:

$$V = \begin{pmatrix} V_{\mathrm{vb}} & 0 \\ 0 & V_{\mathrm{cb}} \end{pmatrix} = \begin{pmatrix} \delta_{\mathrm{v}}\mathcal{T} & 0 \\ 0 & \delta_{\mathrm{c}}\mathcal{T} \end{pmatrix} \tag{10}$$

where δ_{c} and δ_{v} are the parameters governing the strain response for the conduction (V_{cb}) and valence band (V_{vb}) at the K(K') point, respectively. Fig.S.2 shows the calculated conduction band deformation potential, for both 1L and 2L-WSe_2, on a dimer structure with $r = 50$ nm and $H = 200$ nm, along the line connecting the centre of the two nano-pillars. We found a stronger modulation for the bilayer, as expected from the higher strain values shown in Fig.S.1. The potential profile is correlated with the local reduction (increase) of WSe_2 bandgap under tensile (compressive) strain. As such, the maximum tensile deformation, located at the nano-antenna edges, corresponds to a decrease in the conduction band minimum. In correspondence with the compressive strain area, where the layers meet the substrate, the bandagap energy is increased resulting in a potential barrier for free excitons.

SUPPLEMENTARY NOTE II: RAMAN SPECTROSCOPY OF STRAINED 1L-WSE_2

Figure S.3 shows the Raman scattering signal from a monolayer of WSe_2 transferred on top of GaP nano-antennas with different radii, compared to the signal from the planar GaP substrate (black). The 1L-WSe_2 peak at 250 cm^{-1} exhibits a strain-induced shift when deposited on the GaP nano-antennas. The results are consistent with those reported in Ref.[4]. The Raman scattering signal is collected in the setup described in Ref.[5].

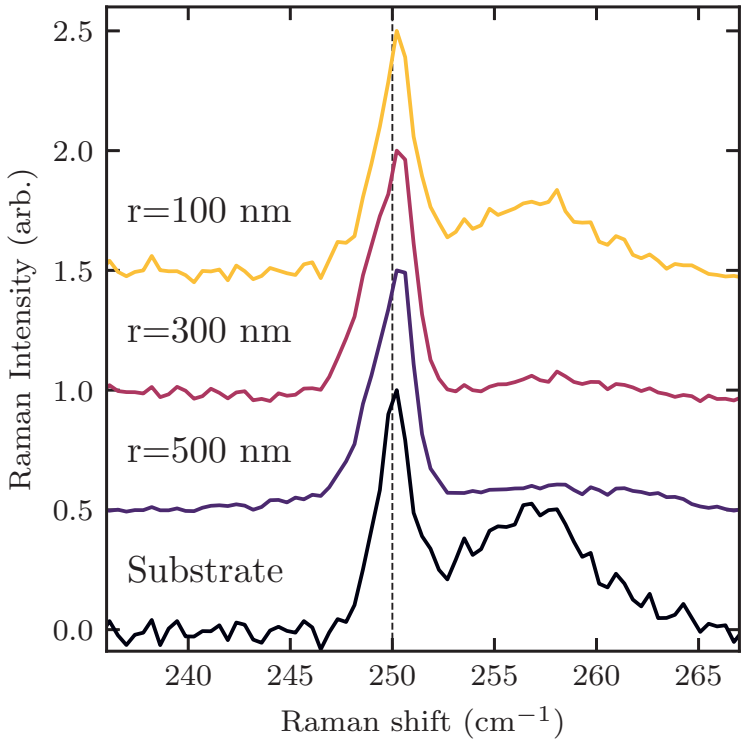

SUPPLEMENTARY FIGURE .3. Raman scattering spectra for 1L-WSe_2 placed on the planar GaP substrate and on different radii nano-antennas. The presence of strain is associated with a shift to higher wavenumber of the main peak at 250 cm^{-1}, corresponding to the $E' + A_1'$ mode. The spectra are normalized and shifted vertically for display.

SUPPLEMENTARY NOTE III: STRAINED 2L-WSe_2 PL EMISSION

To discriminate the relative role of the competing valleys in the transition to a direct bandgap in strained 2L-WSe_2, we extracted the relative emission peak maxima from the PL spectra (as described in Fig.3 of the main text) when deposited on nano-antennas with different radii (Fig.S.4a). The spectra are fitted with two Gaussian functions from which we have extracted their relative energy difference, $\Delta E_{\mathrm{D-I}} = E_{\mathrm{Direct}} - E_{\mathrm{Indirect}}$ (Fig.S.4b). For the unstrained bilayer on the planar GaP substrate we found the largest value of $\Delta E_{\mathrm{D-I}} \approx 80$ meV. When deposited on the nano-antennas, $\Delta E_{\mathrm{D-I}}$ exhibits an initial reduction from the unstrained values, further exhibiting a shift of > 30 meV when approaching the nano-antenna with $r = 50$ nm. Figures S.4c-d show the position of each peak maxima position, as extracted from the 2L-WSe_2 PL spectra collected on nano-antennas with different radii. As the nano-pillar radius is reduced, thus increasing the strain magnitude as shown in Fig.S.1, the E_{Indirect} peak does not exhibits a clear shift in its position when compared to the unstrained case (red circle). On the other hand, we found a large shift of the E_{Direct}, up to a value of approximately 100 meV from the unstrained case. This behaviour confirms the predominant role of the E_{Direct} peak in the indirect-to-direct bandgap transition in 2L-WSe_2 under strain.

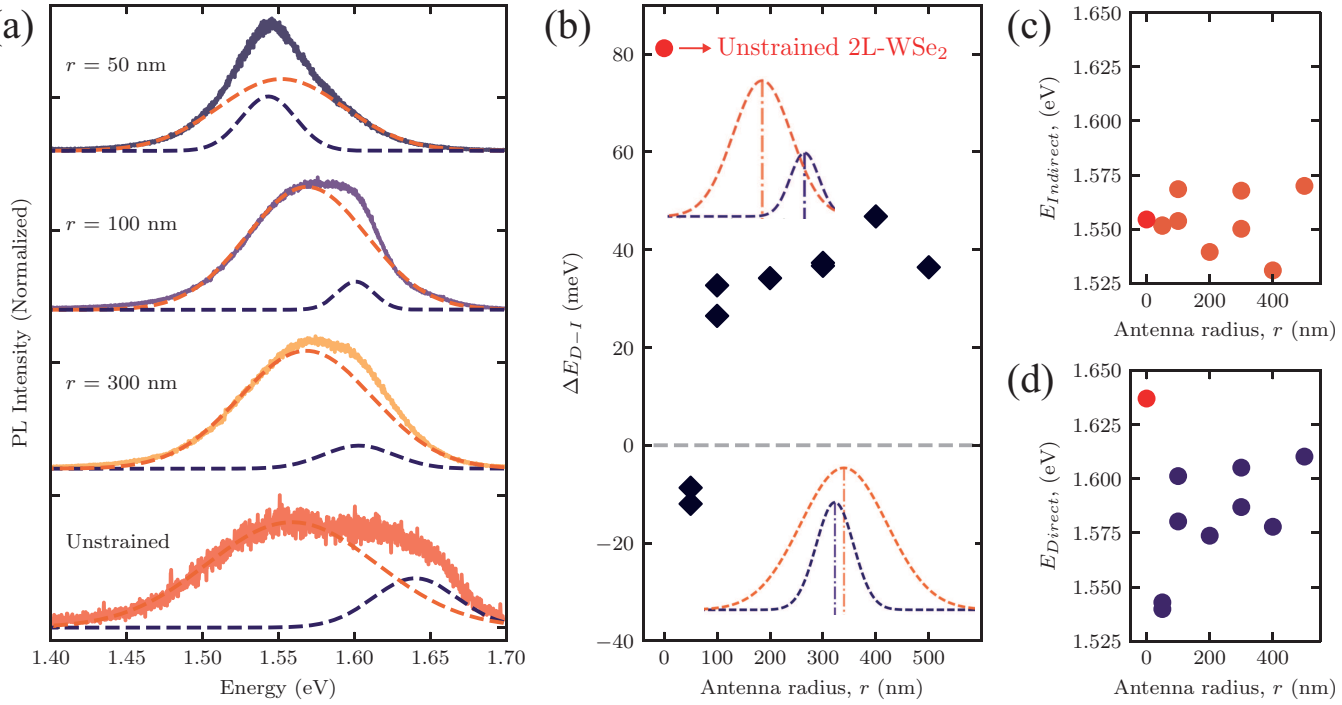

SUPPLEMENTARY FIGURE .4. (a) 2L-WSe_2 PL emission collected on nano-antenna with different radius. The spectra are fitted with two Gaussian peaks relative to the direct (purple) and indirect (orange) transitions. (b) Energy difference ($\Delta E_{\mathrm{D-I}}$) between the direct and indirect peak extracted from the PL emission of 2L-WSe_2 on nanoantennas with different radii. In red the value extracted from unstrained 2L-WSe_2 on planar GaP. The dashed line marks the transition to direct bandgap. (c,d) Direct and indirect peak position (in red for unstrained 2L-WSe_2). No evident change is found in the E_{Indirect} peak (c). In contrast, the E_{Direct} position (d) shows a clear modulation. This effect confirms that a transition to a direct bandgap is caused by the reduction in energy of the $K \rightarrow K$ recombination pathway.

SUPPLEMENTARY NOTE IV: STRAIN-INDUCED 1L-WSE_2 EXCITON RED-SHIFT AT CRYOGENIC TEMPERATURE

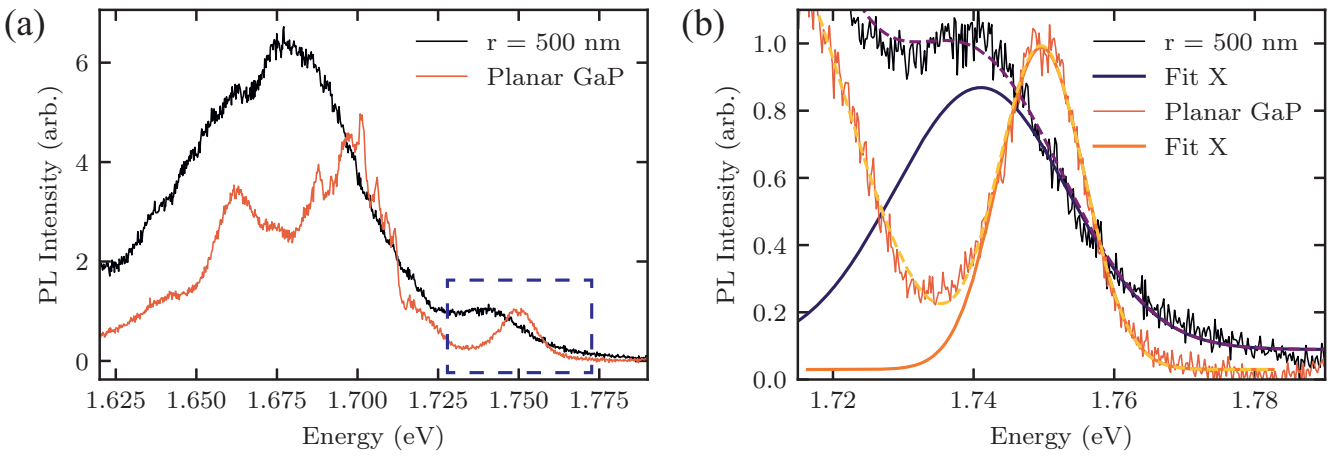

SUPPLEMENTARY FIGURE .5. (a) PL emission of 1L-WSe_2, collected at T=4 K, on the planar GaP substrate (orange) and on a $r = 500$ nm dimer nano-antenna (black). The spectra are normalized to the intensity of the direct exciton emission peak (dashed line box). (b) Gaussian fit of the direct exciton peak for both spectra shown in Fig.S.5a (cumulative fit shown with the dashed line). A red-shift of ≈ 10 meV is observed when on top of the GaP nano-antenna with $r = 500$ nm, consistent with the values extracted at room temperature and with the prediction of our theoretical model.

* l.sortino@sheffield.ac.uk
† a.tartakovskii@sheffield.ac.uk

[1] M. Brooks and G. Burkard, Phys. Rev. B **97**, 195454 (2018).
[2] L. Landau, E. Lifshitz, A. Kosevich, and L. Pitaevski, *Theory of Elasticity* (Elsevier, 1986).
[3] A. J. Pearce, E. Mariani, and G. Burkard, Phys. Rev. B **94**, 155416 (2016).
[4] S. B. Desai, G. Seol, J. S. Kang, H. Fang, C. Battaglia, R. Kapadia, J. W. Ager, J. Guo, and A. Javey, Nano Lett. **14**, 4592 (2014).
[5] L. Sortino, P. G. Zotev, S. Mignuzzi, J. Cambiasso, D. Schmidt, A. Genco, M. Aßmann, M. Bayer, S. A. Maier, R. Sapienza, and A. I. Tartakovskii, Nat. Commun. **10**, 5119 (2019).